

Fluorescence-enhanced optical tomography of a large tissue phantom using point illumination geometries

Ranadhir Roy

Baylor College of Medicine
Photon Migration Laboratory
Houston, Texas 77030

Anuradha Godavarty

Florida International University
Department of Biomedical Engineering
Miami, Florida 33174

Eva M. Sevick-Muraca

Baylor College of Medicine
Photon Migration Laboratory
Houston, Texas 77030

Abstract. We demonstrate fluorescence-enhanced optical imaging of single and multiple fluorescent targets within a large ($\sim 1081 \text{ cm}^3$) phantom using frequency-domain photon migration measurements of fluorescence collected at individual points in response to illumination of excitation light at individual points on the boundary. The tissue phantom was filled with a 1% lipid solution with and without $0.01 \mu\text{M}$ Indocyanine Green (ICG) and targets consisted of vials filled with the 1% lipid containing $1\text{--}2.5 \mu\text{M}$ ICG. Measurements were acquired using a modulated intensified CCD imaging system under different experimental conditions. For 3-D image reconstruction, the gradient-based penalty modified barrier function (PMBF) method with simple bounds constrained truncated Newton with trust region method (CONTN) was used. Targets of 0.5 , 0.6 , and 1.0 cm^3 at depths of $1.4\text{--}2.8 \text{ cm}$ from the phantom surface were tomographically reconstructed. This work demonstrates the practicality of fluorescence-enhanced tomography in clinically relevant volumes.

© 2006 Society of Photo-Optical Instrumentation Engineers. [DOI: 10.1117/1.2338807]

Keywords: Fluorescence-enhanced optical imaging; frequency-domain photon migration; image reconstruction; penalty modified barrier function; constrained truncated Newton method; gradient based.

Paper 05150RR received Jul. 14, 2005; revised manuscript received Apr. 6, 2006; accepted for publication Apr. 7, 2006; published online Aug. 25, 2006.

1 Introduction

Near-infrared (NIR) optical imaging was originally developed for cancer screening based upon the endogenous absorption contrast due to angiogenesis and increased hemoglobin absorbance.^{1–10} Since angiogenesis-induced contrast may be nonexistent or not significant in early metastatic lesions, diagnostic detection may not always be feasible with NIR absorption imaging. In addition, the ability to obtain molecular information from deep, small, and cancer-specific tissue regions from NIR measurement of endogenous absorption alone may have limited diagnostic value. To alleviate these difficulties, exogenous contrast based on targeting and reporting fluorophores may be necessary.^{11–21} Time-dependent boundary measurements have been shown to amplify contrast for fluorescence measurements due to the time delays associated with fluorescence decay kinetics.^{14,15} Yet the reduced signal-to-noise of emission measurements (when compared to absorption imaging at one single wavelength) creates difficulties for tomographic reconstructions in large, clinically relevant volumes.¹⁶

In the past, measured diffuse fluorescence in response to point illumination of continuous wave (CW) excitation light has been acquired for reconstructing contrast-enhanced targets in small volumes (less than 100 cm^3)^{17–21} and, using time-

dependent measurements, in relatively larger volumes (less than 260 cm^3).^{20–24} In these studies, sufficient fluorescence generation and collection across the depth of the entire phantom was possible and hence, three-dimensional image reconstruction was viable. However, in large volumes with deeply positioned fluorescent targets, the fluorescence signal at the boundary may be six orders of magnitude or less than the propagated incident excitation light. In addition, excitation light leakage through interference filters represents a noise floor that decreases the signal-to-noise ratio (SNR) of fluorescent measurements.²⁵ Consequently, the signal-to-noise of the collected fluorescence signal at the boundary decreases with greater target depth and smaller target size in large volumes. Since illumination by excitation light from a single point interrogates a relatively small portion of tissue volume, a series of single pairs of illumination and collection points are required to illuminate the whole tissue volume. Hence, a high density of measurements in a relatively small volume is required for 3-D imaging purposes.

Since the survival chance of breast cancer drops from a rate of about 95% when the lesion is about 0.5 cm in size to a rate of 75% when the cancer is treated at a size of about 2.5 cm ,²⁶ a successful reconstruction algorithm must enable reconstruction of targets as small as 0.5 cm at different tissue depths in order for fluorescence-enhanced optical tomography to be clinically relevant. Hence, one of our main objectives of

Address all correspondence to: Ranadhir Roy, Dept. of Radiology, Baylor College of Medicine, One Baylor Plaza - BCM 360, Houston, TX 77030; Tel: 713-798-4417; Fax: 713-798-8050; E-mail: ranadhir@bcm.tmc.edu

this study is to reconstruct the target as small as 0.5 cm at a depth of 2.8 cm using phantom data. Reconstruction of smaller targets may be possible by incorporating an adaptive finite element technique.²⁷ Reconstructions of multiple targets mimic the clinically relevant situation of metastatic spread and also are a hallmark of fluorescence-enhanced optical tomography.

Previously, we have developed an image reconstruction algorithm based on the penalty modified barrier function (PMBF) method with simple bound constraint technique (CONTN) and applied for reconstruction of an immersed fluorescent target following area illumination with modulated excitation light.²⁸ In this paper, the same PMBF/CONTN algorithm is used for fluorescence measurements acquired from a breast-shaped phantom containing single and multiple targets that are illuminated with points of modulated excitation light (100 MHz) on the boundary surface. In this approach, a forward problem described by the coupled diffusion equations with assumed optical properties of the phantom is solved by the finite element method to predict the fluorescence measurements on the boundary. The PMBF with the constrained truncated Newton with trust region method (CONTN) is then used within the inverse problem to update the values of the optical properties of the phantom that minimizes the errors between the boundary measurements and those calculated from the forward problem. The PMBF/CONTN algorithm is gradient-based, and the gradients are calculated accurately and efficiently by reverse automatic differentiation technique enabling its use for large problems.²⁹ Furthermore, since we employ a methodology to compute the Lagrange multiplier parameters that essentially regularize the solution, there is no *a priori* information required, and the potential for committing the “inverse crime” is avoided.

It is well known that Tikhonov regularization is used for ill-posed inverse problem like optical tomography problems. In the Tikhonov technique, the Lagrange parameter is introduced to make the inverse problem well-posed, i.e., improving the condition number of the Hessian matrix. The Tikhonov regularization method does not allow imposition of physical constraints but does allow mathematical constraints. The PMBF/CONTN method uses the Lagrange multipliers similar to the Tikhonov method but allows physical constraints. The main object of this study is to investigate whether our algorithm can reconstruct images from measurement data using heterogeneities of different volumes and at different depths under perfect and imperfect uptake conditions including

1. when the heterogeneity is 1.0 to 2.8 cm deep from the surface,
2. when the volume of the heterogeneity is as small as 0.5 cm³ (spherical), and
3. when there are multiple heterogeneities as in our example where three spherical heterogeneities (~0.55 cm³) are located at depths of 1.2 to 1.4 cm.

In the following, the phantom and the measurement technique using point illumination/point collection are briefly described. The PMBF/CONTN algorithm for fluorescence-enhanced tomography is next described and the reconstructed images that demonstrate three-dimensional optical tomographic recon-

Point illumination geometry

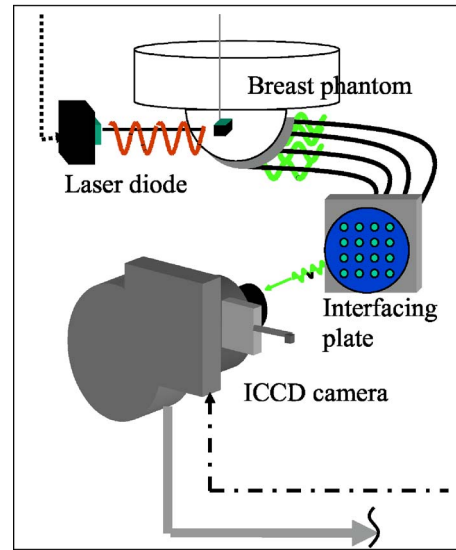


Fig. 1 Schematic showing point illumination and point collection of a breast-shaped phantom with the cup-shaped portion (10-cm diameter) representing the breast tissue, and the cylindrical portion (20-cm diameter and 2.5-cm height) representing the extended chest wall region around the breast. Phantom set-up including collection fibers that are interfaced to the hemispherical surface of the phantom on one end, and to either of two interfacing plates on the other end.

struction on a large tissue phantom using point illumination/collection are presented within the Results and Discussion section.

Finally, this work shows the ability to use the PMBF/CONTN algorithm in different measurement geometries that was previously displayed to reconstruct 3-D interior images of targets from area illumination/detection geometries.²⁸ The lack of need for *a priori* parameters enables algorithm performance in both areas as well as point illumination geometries.

2 Materials and Methods

2.1 The Phantom Using Point Illumination/Point Collection Geometry

In this study, image reconstructions were performed using measured fluorescent light intensity and phase-shift acquired on the surface of a breast-shaped phantom as shown in Fig. 1. The hemispherical portion of the phantom (10-cm diameter) represents the breast tissue and the cylindrical portion (20-cm diameter and 2.5-cm height) represents the extended chest wall regions. Point illumination and point collection geometry was used to acquire data using optical fibers of 1-mm diameter that were located in concentric rings along the hemispherical surface of the phantom. The tissue phantom was filled with a 1% Liposyn solution to mimic the scattering properties of tissue. Different spherical target volumes (0.5 and 1.0 cm³) were filled with the 1% lipid containing 1 μ M Indocyanine Green as the fluorophore. The targets were placed 1.4–2.8 cm deep within the phantom (for further details on the phantom and measurement geometry, see Refs. 30–32). The optical properties of the background and targets used in these experiments are given in Table 1. In experiments

Table 1 Optical properties of target and surroundings in perfect and imperfect data measurement sets.

| Optical properties | Perfect uptake | | Imperfect uptake | |
|---|----------------|-------------------------|------------------|---------------|
| | Target | Background | Target | Background |
| Excitation ^a $\mu_{\sigma_{xf}} + \mu_{\sigma_{xi}}$ (cm ⁻¹) Experiments 1-7 | 0.30+0.0248 | 0.0+0.0248 ^c | 0.30+0.0248 | 0.003+0.0248 |
| Emission ^a $\mu_{\sigma_{mf}} + \mu_{\sigma_{mi}}$ (cm ⁻¹) Experiments 1-7 | 0.050+0.0332 | 0.0+0.0322 | 0.05+0.0332 | 0.0005+0.0332 |
| Excitation ^b $\mu_{\sigma_{xf}} + \mu_{\sigma_{xi}}$ (cm ⁻¹) Experiments 8 | 0.750+0.0248 | 0.0+0.0248 | none | none |
| Emission ^b $\mu_{\sigma_{mf}} + \mu_{\sigma_{mi}}$ (cm ⁻¹) Experiments 8 | 0.130+0.0332 | 0.0+0.0322 | none | none |

^aConcentration of ICG 1 μ M.

^bConcentration of ICG 2 μ M.

^cThe value for example, 0.0 represents the optical property $\mu_{\sigma_{xf}}$ and the value 0.0248 represents the optical property $\mu_{\sigma_{xi}}$ where the total summation of $\mu_{\sigma_{xf}} + \mu_{\sigma_{xi}}$ is equivalent to the total absorption properties. This is our attempt to distinguish absorption due to fluorophore, $\mu_{\sigma_{xp}}$ and absorption due to chromophore, $\mu_{\sigma_{xi}}$ in the phantom.

$\mu_{\sigma_{xf}}$, $\mu_{\sigma_{xi}}$: Absorption coefficient due to the fluorophore and chromophore at excitation wavelength.

$\mu_{\sigma_{mf}}$, $\mu_{\sigma_{mi}}$: Absorption coefficient due to the fluorophore and chromophore at emission wavelength.

Lifetime, τ , was 0.56 ns; quantum efficiency, ϕ , was 0.016; and the isotropic coefficients at the excitation, μ_{sx} and emission, μ_{sm} wavelength were 10.88 and 9.82 cm⁻¹, respectively.

#1-7, 1 μ M ICG was used in the spherical target while in experiment #8, three \sim 0.5 cc spherical targets containing 2.5 μ M ICG were positioned within the background containing no ICG.

2.2 Measurement Approach

Time-dependent emission measurements reflecting light propagation and decay kinetics were made using frequency-domain techniques. The phantom was sequentially illuminated at a single point on the phantom surface with intensity modulated excitation light (783 nm at 100 MHz modulation frequency) using 1000- μ m diameter fiber optics to deliver excitation light. The fluorescent signal (830 nm) was collected from point locations on phantom surface via 1000- μ m diameter optical fibers. Interference (830 nm) and holographic filters were used to block the excitation light. The light emitted from the ends of all collecting fibers were simultaneously collected using a gain-modulated intensified charge coupled device (ICCD) camera that was operated in homodyne mode. That is, the ICCD camera was used for simultaneous data acquisition from multiple collection fibers that were interfaced as 2-D arrays onto an interfacing plate to collect emission AC intensity I_{AC_m} and emission phase-shift θ_m . Fluorescent measurements were acquired following illumination at single points, where the data used for reconstruction had an average fluorescent modulation depth (AC/DC) greater than 0.1.

2.3 Imaging Trials Conducted

Experiments were conducted under different experimental conditions in which the fluorescent contrast of the target to background ratio (Target:Background=T:B) was either 1:0 or

100:1. In the case of perfect uptake (T:B=1:0), the objective was to detect fluorescent targets in an otherwise nonfluorescent background as may be the case for sentinel lymph node mapping. Here the fluorescent contrast agent may be injected peritumorally for uptake and mapping of the lymph flow to the major nodes in the body, and the background is essentially nonfluorescent. In the case of imperfect uptake (T:B=100:1), the objective was to mimic the optical contrast for systemically administered, molecularly targeting fluorescent contrast agents. When systemically administered, the agent is typically distributed in the background as well as within the target. We initially employ an optimal T:B ratio of 100:1 due to experimental limitations described ahead in the Discussion section.

Measurements were performed with a single spherical target of 0.5 cm³ or 1.0 cm³ volume at depths ranging from 1.4 to 2.8 cm from the phantom surface (based upon the centroid of the target). Measurements were also performed with multiple spherical targets of 0.5-0.6 cm³ volumes at approximately 1.4-cm distance from the phantom surface. In summary, eight experiments were conducted for tomographic reconstruction as described in Tables 1 and 2. The number of fluorescence intensity I_{AC_m} and phase shift θ_m measurements made on the surface of the phantom for image reconstruction from each experiment are also given in Table 2.

A reference scheme was used in this experimental data to reduce the instrument effects and the unknown source strength.^{24,33} In the reference scheme, the emission fluences, Φ_m , from multiple collection fiber locations were referenced with respect to the emission fluence data from a single specified reference collection fiber (*ref*) as given in Eq. (1):

Table 2 Experimental conditions, number of targets, location of targets, number of experimental measurements, relative model mismatch error of amplitude ($E_{I_{AC}}$) phase-shift (E_θ), and number of unknowns of the inverse problems using Mesh 1 (coarse mesh) and Mesh 2 (fine mesh).

| Expt. | Target | Depth (cm) | Target vol. (cm ³) | Ratio (T:B) | Number of measurements | Number of mismatch error more than 50% | | |
|-------|--------|------------|--------------------------------|--------------------|------------------------|--|--------------|-------------------|
| | | | | | | $E_{I_{AC}}^c$ | E_θ^d | Mesh ^e |
| 1 | 1 | 1.4 | 1 | 1:0 ^a | 547 | 165 | 201 | 1 |
| 2 | 1 | 1.4 | 1 | 100:1 ^b | 388 | 126 | 218 | 1 |
| 3 | 1 | 2.0 | 1 | 1:0 ^a | 180 | 94 | 128 | 1 |
| 4 | 1 | 2.0 | 1 | 100:1 ^b | 466 | 380 | 389 | 1 |
| 5 | 1 | 2.8 | 1 | 1:0 ^a | 145 | 88 | 90 | 1 |
| | | | | | | 68 | 108 | 2 |
| 6 | 1 | 2.8 | 1 | 100:1 ^b | 468 | 266 | 249 | 1 |
| | | | | | | 232 | 236 | 2 |
| 7 | 1 | 2.8 | ~0.5 | 1:0 ^a | 334 | 134 | 113 | 1 |
| | | | | | | 123 | 100 | 2 |
| 8 | 3 | 1.2-1.4 | ~0.55 | 1:0 ^a | 276 | 145 | 72 | 1 |
| | | | | | | 120 | 100 | 2 |

^aTarget:background ratio of absorption due to fluorophore (1:0). Perfect uptake condition.

^bTarget:background ratio of absorption due to fluorophore (100:1). Imperfect uptake condition.

^cRelative model mismatch error of amplitude $E_{I_{AC}}$ (Eq. (8)).

^dRelative model mismatch error of phase-shift E_θ (Eq. (9)).

^eMesh 1 (coarse) 6956 nodes, 34,413 tetrahedral elements (unknowns 6956), Mesh 2 (fine) 18,105 nodes, 94,767 tetrahedral elements (unknowns 18,105).

$$\frac{(\Phi_m)_p}{(\Phi_m)_{ref}} \quad p = 1, \dots, N_B \quad (1)$$

where p is the position of collection on the surface of the phantom and N_B is the number collecting fibers on the surface. Thus, the relative phase shift and AC ratio were calculated from the difference in phase [i.e., $(\Delta\theta_m)_p = (\theta_m)_p - (\theta_m)_{ref}$] and the ratios of amplitude [i.e., $(\Delta I_{AC_m})_p = (I_{AC_m})_p / (I_{AC_m})_{ref}$]. The location of the reference positions were selected for each source, as the reference measurement was taken at least 2 cm away from the point of excitation illumination.³⁰

2.4 The Forward Problem to Predict Intensity (I_{AC}) and Phase-Shift (θ) on Boundary Points

The diffusely propagated fluorescence in response to excitation illumination is predicted by the coupled diffusion Eqs. (2) and (3):

$$-\nabla \cdot [D_x(\vec{r}) \nabla \Phi_x(\vec{r}, \omega)] + \left[\frac{i\omega}{c} + \mu_{a_x}(\vec{r}) + \mu_{a_{xf}}(\vec{r}) \right] \Phi_x(\vec{r}, \omega) = S \quad \text{on } \Omega \quad (2)$$

$$-\nabla \cdot [D_m(\vec{r}) \nabla \Phi_m(\vec{r}, \omega)] + \left[\frac{i\omega}{c} + \mu_{a_m}(\vec{r}) \right] \Phi_m(\vec{r}, \omega) = \phi \mu_{a_{xf}} \frac{1}{1 - i\omega\tau} \Phi_x(\vec{r}, \omega) \quad \text{on } \Omega \quad (3)$$

Here, Φ_x and Φ_m are the AC components of the excitation and emission photon fluence (photons/cm²/sec) at position \mathbf{r} , respectively; ω is the angular modulation frequency (rad/s); c is the speed of light within the medium (cm/s); $\mu_{a_{xi}}$ is the absorption due to chromophores (cm⁻¹); and $\mu_{a_{xf}}$ is the absorption due to fluorophores (cm⁻¹). $D_{x,m}$ is the optical diffusion coefficient equivalent to $1/3(\mu_{a_{x,m}} + \mu'_{s_{x,m}})$, where $\mu'_{s_{x,m}}$ is the isotropic scattering coefficient (cm⁻¹) and $\mu_{a_{x,m}}$ is the total absorption coefficient, at the respective wavelengths. The total absorption at the emission wavelength μ_{a_m} is equal to the absorption due to nonfluorescent chromophore $\mu_{a_{xi}}$ and fluorescent chromophores $\mu_{a_{mf}}$. The right-hand term of Eq. (2) describes the generation of fluorescence within the medium. The term ϕ represents the quantum efficiency of the fluorescence process, which is defined as the probability that an excited fluorophore will decay radiatively, and τ is the fluorophore lifetime (ns). The numerical solutions for the excitation

and emission fluence distributions given in Eqs. (2) and (3) are obtained using the Robin boundary condition.³⁴ The Galerkin finite element method with tetrahedral elements was used to solve differential Eqs. (2) and (3). From the solution of Φ_m , the values of the amplitude, I_{AC_m} , and phase shift, θ_m , can be determined from the relationship

$$\Phi_m = I_{AC_m} \exp(i\theta_m) \quad (4)$$

Two finite elements meshes were employed for the forward problem. The first contained 6956 nodes with 34,413 tetrahedral elements (denoted below as Mesh 1) while the second, more refined mesh contained 18,105 nodes with 94,767 tetrahedral elements (defined as Mesh 2). This second mesh was used to demonstrate the impact of discretization of image resolution and accuracy. Twenty-seven seconds and 253 seconds of CPU time were required to solve the coupled excitation and emission equations for Mesh 1 and Mesh 2, respectively. All the computations were performed in double precision on a SUN-blade 100 UNIX workstation.

2.5 Formulation for Image Reconstruction

The starting point for formulating the reconstruction as an optimization problem begins with defining the error function $E(\mu_{a_{xf}}, \omega)$,

$$E(\mu_{a_{xf}}, \omega) = \frac{1}{2} \sum_{p=1}^{N_B} [(\log(Z_p)_{cal} - \log(Z_p)_{mea})(\log(Z_p)_{cal}^* - \log(Z_p)_{mea}^*)] \quad (5)$$

subject to the constraint $\{l \leq \mu_{a_{xf}} \leq u\}$, where l is the lower and u is the upper bounds of $\mu_{a_{xf}}$ given as n vector. For optical tomography problems, the user can specify range, i.e., the lower and upper bounds, for each variable based on physical consideration. In Eq. (5), cal denotes the value calculated by the forward problem, mea denotes the experimental measured values, and N_B is the number of detectors. The superscript * denotes the complex conjugate of the complex number Z_p . Z_p is comprised of the referenced fluorescent amplitude, $I_{AC_{ref_p}}$, and the referenced phase shift θ_{ref_p} measured at boundary point, p , in response to point illumination. Specifically, the referenced measurement at boundary point p was given by

$$Z_p = I_{AC_{ref_p}} \exp(i\theta_{ref_p}) \quad (6)$$

where

$$I_{AC_{ref_p}} = \frac{I_{AC_p}}{I_{AC_{max}}}; \quad \theta_{ref_p} = \theta_p - \theta_{atI_{AC_{max}}}$$

The reference scheme for the calculated data, $(Z_p)_{cal}$ was the same as that used for the measured data, $(Z_p)_{mea}$.

In the inverse problem, the selection of the error function [as given by Eq. (5)] is important, because it determines how the measurements are related to the model. The fluence, $\Phi_m = I_{AC} e^{i\theta}$, has been chosen because it contains all the available information and can be related to the observable measurements of amplitude intensity, I_{AC} , and phase shift, θ . Since absolute measurements are not practical to acquire due to in-

strumentation effects and inability to calibrate each source, the measurement data and the calculated fluence were normalized as given in Eq. (1). The error function provides the difference between the normalized measurement and normalized computed fluence. We take the difference of the log of measured and computed normalized values since it results in a difference in phase and ratio of amplitude. We find this approach most effective. Since comparison of the difference of two complex values is difficult to translate into any physical meaning, the complex conjugate is introduced in Eq. (5) to ensure the error function is a real-valued norm.

The constrained truncated Newton with trust region (CONTN) method^{35,36} and the nonlinear conjugate method were used to optimize the error function [Eq. (5)] using the measured data. While target reconstructions were obtained using simulated data,^{35,36} these methods failed to reconstruct targets when using experimental data. The most popular method for illconditioned problems is to use Tikhonov's regularization technique.³⁷ The difficult and time-consuming task in Tikhonov regularization is to find the value of the regularization parameter given ground truth, something which is not available in true imaging situations. Hence, the PMBF/CONTN method was developed as described in Ref. 28. A brief description is contained in the following:

In the PMBF method, we use the modified barrier penalty function, M (termed hereafter as the barrier function), to incorporate the constraints directly within the optimization variable:^{28,38-40}

$$\min_{\mu_a} M(\mu_{a_{xf}}, \lambda, \eta) = E(\mu_{a_{xf}}) - \eta \sum_{i=1}^n \lambda_i^l f_i(\mu_{a_{xf}_i} - l) + \lambda_i^u f_i(u - \mu_{a_{xf}_i}) \quad (7)$$

where η is a penalty/barrier term, n is the number of nodal points, λ^l and λ^u are vectors of Lagrange multipliers for the bound constraints for the lower and upper bounds, respectively. From Eq. (7) one can see that the simple bounds are included in the barrier function M . The function f and Lagrange multiplier λ are described elsewhere.²⁸

The PMBF method is performed in two stages within an inner and an outer iteration. The outer iteration updates the Lagrange multiplier, λ . Formulations used to update these parameters at each outer iteration are provided in Ref. 28. Using the calculated values of the parameters λ and f , CONTN is applied to minimize the penalty barrier function described by Eq. (7). Once satisfactory convergence within the inner iteration reached, the Lagrange multipliers, λ , and the barrier parameter, η , are updated in outer iteration and another constrained optimization is started within the inner iteration. A precise description on the PMBF/CONTN algorithm is provided in Ref. 28. Herein we also use the modified method of Breitfeld and Shanno³⁹ for initializing the Lagrange multipliers without *a priori* information. This effectively removes the need to choose an appropriate initial values of the Lagrange multipliers based upon ground truth, which in actual imaging is not known. The success of the algorithm depends upon the consistent convergence of both inner and outer iteration loops.

2.6 Evaluation of Reconstructed Images

2.6.1 Model mismatch

In a phantom study it is possible to find the mismatch between “ground truth” and the discretized finite element method predictions given the true conditions specified in Table 1. This information provides the model mismatch error and enables examination of whether the PMBF/CONTN algorithm can reconstruction images given a known level of model mismatch errors. The relative model mismatch error of referenced amplitude and referenced phase shift are calculated at each detector point p , on the surface of the phantom using the following equations:

$$(E_{I_{AC}})_p = \left(\frac{(I_{AC_{ref}})_{mea} - (I_{AC_{ref}})_{cal}}{(I_{AC_{ref}})_{cal}} \right)_p \times 100\%, \quad (8)$$

$$p = 1, \dots, N_B$$

$$(E_{\theta})_p = \left(\frac{(\theta_{ref})_{mea} - (\theta_{ref})_{cal}}{(\theta_{ref})_{cal}} \right)_p \times 100\%, \quad (9)$$

$$p = 1, \dots, N_B$$

2.6.2 Merits of reconstruction algorithm

Both qualitative (visual) agreement and quantitative figures of merit were used to assess the accuracy of the optimization techniques. The root mean squares were calculated:

$$RMSE = \sqrt{\frac{1}{n} \sum_{i=1}^n [(\mu_{a_{xf}})_{true} - (\mu_{a_{xf}})_{cal}]^2} \quad (10)$$

where n is the number of nodal points in the finite element mesh. The RSME criteria would not be possible to apply in clinical situations because no true image is known. However, the RSME criteria provide the principal advantage of conducting evaluation of our algorithm using phantom data.

3 Results and Discussion

3.1 Model Mismatch Error

The number of measurements in which the relative model mismatch errors of fluorescent amplitude ($E_{I_{AC}}$) and phase shift (E_{θ}) were greater than 50% is given in Table 2. In all the experiments, the relative model mismatch errors of the amplitude are lower than that of phase shift. From Table 2, it can be seen that

1. the percentage number of relative model mismatch errors greater than 50% was less for the perfect uptake case compared to that of the imperfect uptake,
2. the percentage number of relative model mismatch errors greater than 50% was less for Mesh 2 compared to that of Mesh 1,
3. the percentage number of relative model mismatch errors greater than 50% was increased considerably as the target depth increased from 1.4 cm to 2.8 cm from the surface.

The relative mismatch errors are shown in Figs. 2 and 3 for experiment #1 using Mesh 1. Figures 2 and 3 show histo-

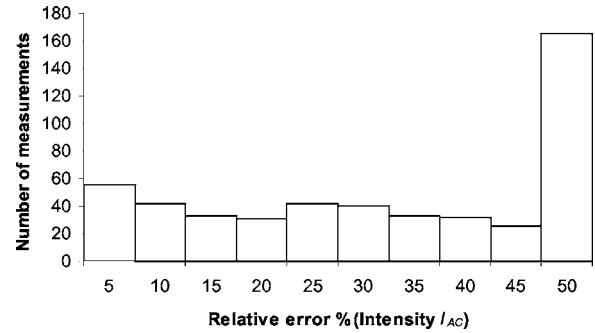


Fig. 2 Histogram of relative model mismatch error, $E_{I_{AC}}$, defined by Eq. (8) of fluorescence reference intensity $I_{AC_{ref}}$ for experiment #1.

grams of the relative mismatch error of referenced fluorescent amplitude intensity, $I_{AC_{ref}}$, and referenced phase shift θ_{ref} , respectively. The reasons for such errors are discussed in detail in Refs. 30 and 31, but briefly they reflect discretization, measurement, and experimental error.

3.2 Target Depth Study (Single Spherical 1-cm³ Target)

The absorption coefficient due to the fluorescent, $\mu_{a_{xf}}$, was reconstructed for the experiments #1–6. Figure 4 illustrates the PMBF/CONTN recovery of absorption coefficient due to fluorescence from referenced fluorescent measurements in experiment #1 made under perfect uptake conditions. Similar imaging results were obtained for experiments #2–6 for brevity, results are not shown. Tables 3 and 4 summarize all the computed runs of experiments #1–6. In this set of reconstructions, the lower and the upper bounds were chosen to be 0.003 cm⁻¹ and 0.3 cm⁻¹, respectively. Since the known amount of fluorophore was introduced, we can specify a lower bound greater than zero, and an upper bound of some practical value. Figure 4(a) represents the actual spatial distribution of fluorescence absorption coefficient, $\mu_{a_{xf}}$, in $Z=2.4$ -cm plane through the target when a target centroid of volume 1.0 m³ was located at 0.5, -2.5, and 2.5 cm away from the surface (experiment #1) while Fig. 4(b) shows the reconstructed target in $Z=2.4$ -cm plane through the target using an initial guess of uniform $\mu_{a_{xf}}^0$ to be 0.003 cm⁻¹ and the initial Lagrange multipliers set to $\lambda_i^0=1000$ for perfect uptake condition. The reconstructed targets using the initial Lagrange multiplier set to $\lambda_i^0=1, 10,$ and 100 were identifiable (for

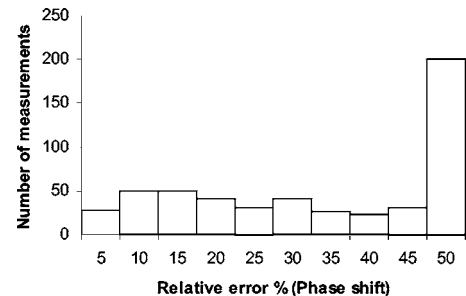


Fig. 3 Histogram of relative model mismatch error, E_{θ} , defined by Eq. (9) of fluorescence reference phase-shift θ_{ref} for experiment #1.

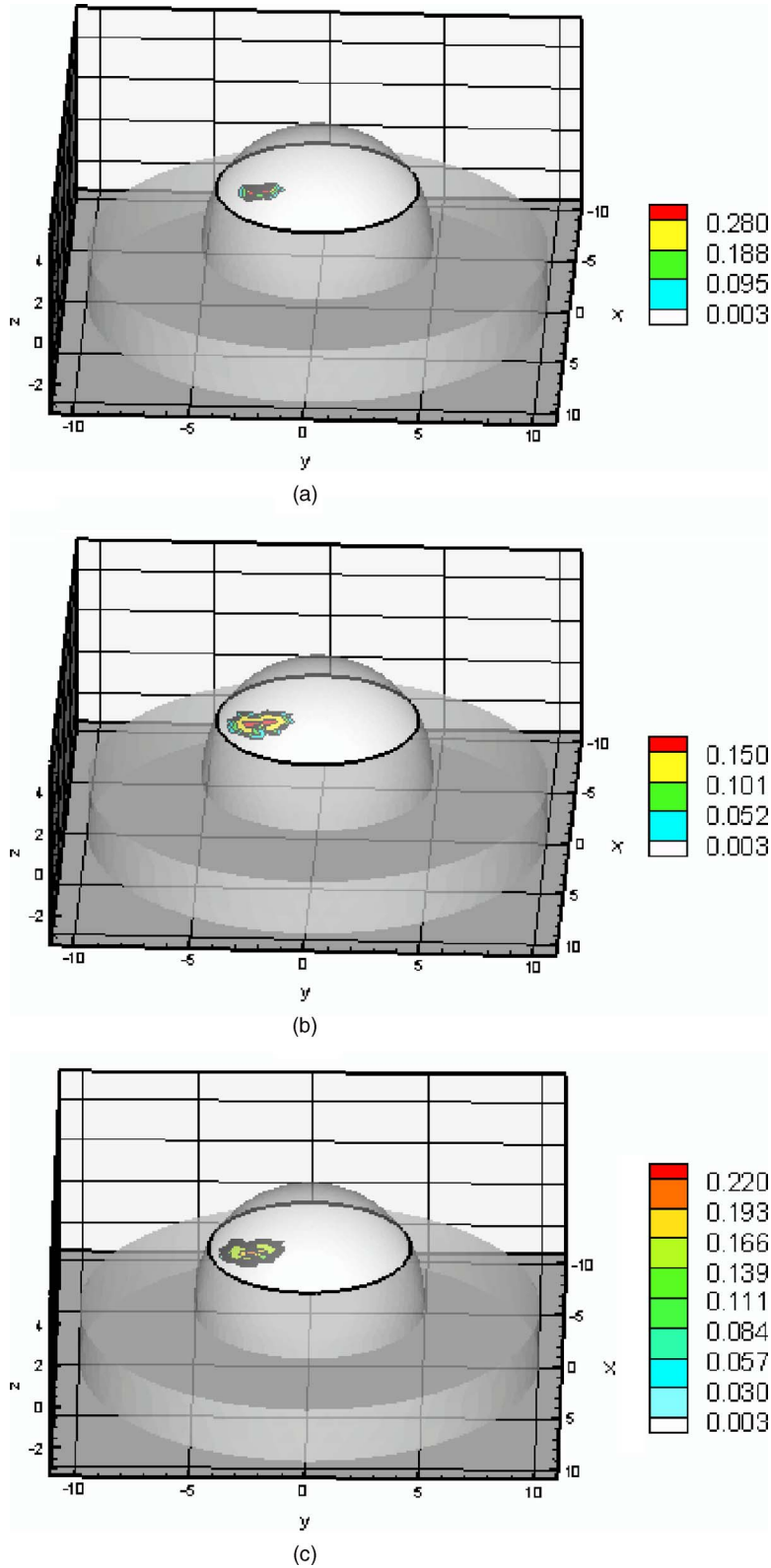


Fig. 4 Distribution of absorption coefficient due to fluorophore $\mu_{a,xf}$ cm^{-1} with 1.0 cm^3 spherical target located at 1.4 cm deep from the surface (centroid, $0.5, -2.5, 2.5$) under perfect uptake condition at $Z=2.4\text{-cm}$ plane through the target, (a) actual distribution of the absorption coefficient due to fluorophore, (b) reconstructed image using initial value $\mu_{a,xf}^0=0.003 \text{ cm}^{-1}$ and $\lambda^0=1000$, (c) reconstructed image using initial value $\mu_{a,xf}^0=0.003 \text{ cm}^{-1}$ and calculated λ^0 (experiment #1, Mesh 1).

Table 3 Summary of figures of targets reconstruction, CPU time and the root mean square error (RMSE) as a function of initial value of the absorption coefficient due to fluorophore $\mu_{a,xf}^0 = 0.003$ and the initial Lagrange multiplier $\lambda^0 = 1000$ as well as calculated λ^0 (Ref. 28) for perfect and imperfect uptake measurement (experiments #1–4) using Mesh 1.

| Exp. | Lagrange λ^0 | Time (min.) | Centroid [xyz] (cm) | RMSE ^b | Mesh ^c | Volume (cm ³) | Max ^f $\mu_{a,xf}$ (cm ⁻¹) |
|----------------|----------------------|-------------|---------------------|-------------------|-------------------|---------------------------|---|
| 1 ^d | Actual | | 0.5–2.5 2.5 | | 1 | 1.0 | 0.3 |
| | $\lambda^0 = 1000$ | 44 | 0.5–2.5 2.5 | 0.0133 | 1 | 2.1 | 0.24 |
| | Cal λ^{0a} | 60 | 0.5–2.5 2.5 | 0.0122 | 1 | 2.1 | 0.17 |
| 2 ^d | Actual | | 0.5–2.5 2.5 | | 1 | 1.0 | 0.3 |
| | $\lambda^0 = 1000$ | 25 | 0.5–2.5 2.5 | 0.0128 | 1 | 2.8 | 0.17 |
| | Cal λ^{0a} | 34 | 0.5–2.5 2.5 | 0.0123 | 1 | 2.5 | 0.11 |
| 3 ^d | Actual | | 0.5–1.4 2.5 | | 1 | 1.0 | 0.3 |
| | $\lambda^0 = 1000$ | 20 | 0.4–1.4 2.6 | 0.0122 | 1 | 1.9 | 0.17 |
| | Cal λ^{0a} | 29 | 0.4–1.4 2.6 | 0.0116 | 1 | 1.9 | 0.17 |
| 4 ^d | Actual | | 0.5–1.4 2.5 | | 1 | 1.0 | 0.3 |
| | $\lambda^0 = 1000$ | 33 | 0.4–1.4 2.6 | 0.0113 | 1 | 1.9 | 0.16 |
| | Cal λ^{0a} | 40 | 0.4–1.4 2.6 | 0.0111 | 1 | 1.9 | 0.17 |
| 1 ^e | Actual | | 0.5–2.5 2.5 | | 1 | 1.0 | 0.3 |
| | Cal λ^{0a} | 82 | 0.5–2.5 2.5 | 0.0194 | 1 | 2.7 | 0.27 |

^aUsing calculated Lagrange multiplier λ_i^0 (Ref. 28).

^bRoot mean square error (RMSE, Eq. (10)).

^cMesh 1 (coarse) with 6956 nodes, Mesh 2 (fine) with 18,105 nodes.

^dLower and upper bound (0.003, 0.3).

^eLower and upper bounds (0.002, 0.4).

^fMaximum absorption coefficient due to fluorophore in the target region.

brevity data not shown) but were consistently smaller in size than the actual target. In addition, the locations of the targets were shifted from the actual target position toward the illumination surface without the reconstruction of artifacts. Our results were the same with different initial values of $\mu_{a,xf}^0$, if of course the initial values of $\mu_{a,xf}^0$ were chosen between the lower and upper bounds. To choose an initial value that violates these bounds violates the physics of the problem. Figure 4(c) shows the reconstructed target in $Z=2.4$ -cm plane using the initial value of λ_i^0 computed using the method of Breitfeld and Shanno.³⁹ It is seen from Fig. 4 that the reconstructed targets are clearly identifiable and the shapes of the reconstructed targets are slightly larger than the true target. Similar trends were observed for other experiments as given in Tables 3 and 4. Nonetheless it is found that it was not necessary to find the initial values of the Lagrange multiplier λ_i^0 by comparison with ground truth on a trial-and-error basis; but instead we could use the simple least-squares procedure to compute these values. Similar phenomena were observed when this reconstruction algorithm was applied to a phantom study using area illumination/collection geometry.²⁸

Ten inner iterations and 10 outer iterations were required to reconstruct these images. The reconstructed images did not improve when we increased the number of inner iterations to 20 and outer iterations to 20. The total CPU time required with the different initial values of the Lagrange multipliers are given in Tables 3 and 4. It can be seen that less CPU was required when the initial Lagrange multipliers were chosen to be, $\lambda^0 = 1000$ than when the values of λ^0 were calculated.

For quantitative analysis of the reconstructed images, values of the RMSE are listed in Tables 3 and 4. The RMSE values are small when the initial Lagrange multipliers were chosen to be $\lambda^0 = 1000$. The RSME values improved further when the initial Lagrange multipliers were calculated. Estimation of the target centroid with respect to the true centroid is tabulated in Tables 3 and 4. The targets were reconstructed close to their true locations with no artifacts as shown in Fig. 4. In the cases of the perfect or imperfect experiments, the reconstructed depth targets were not underestimated as depth of the target increased from 1 cm to 2.8 cm.

These figures show that the PMBF/CONTN method is stable and accurate given the number of iterations required.

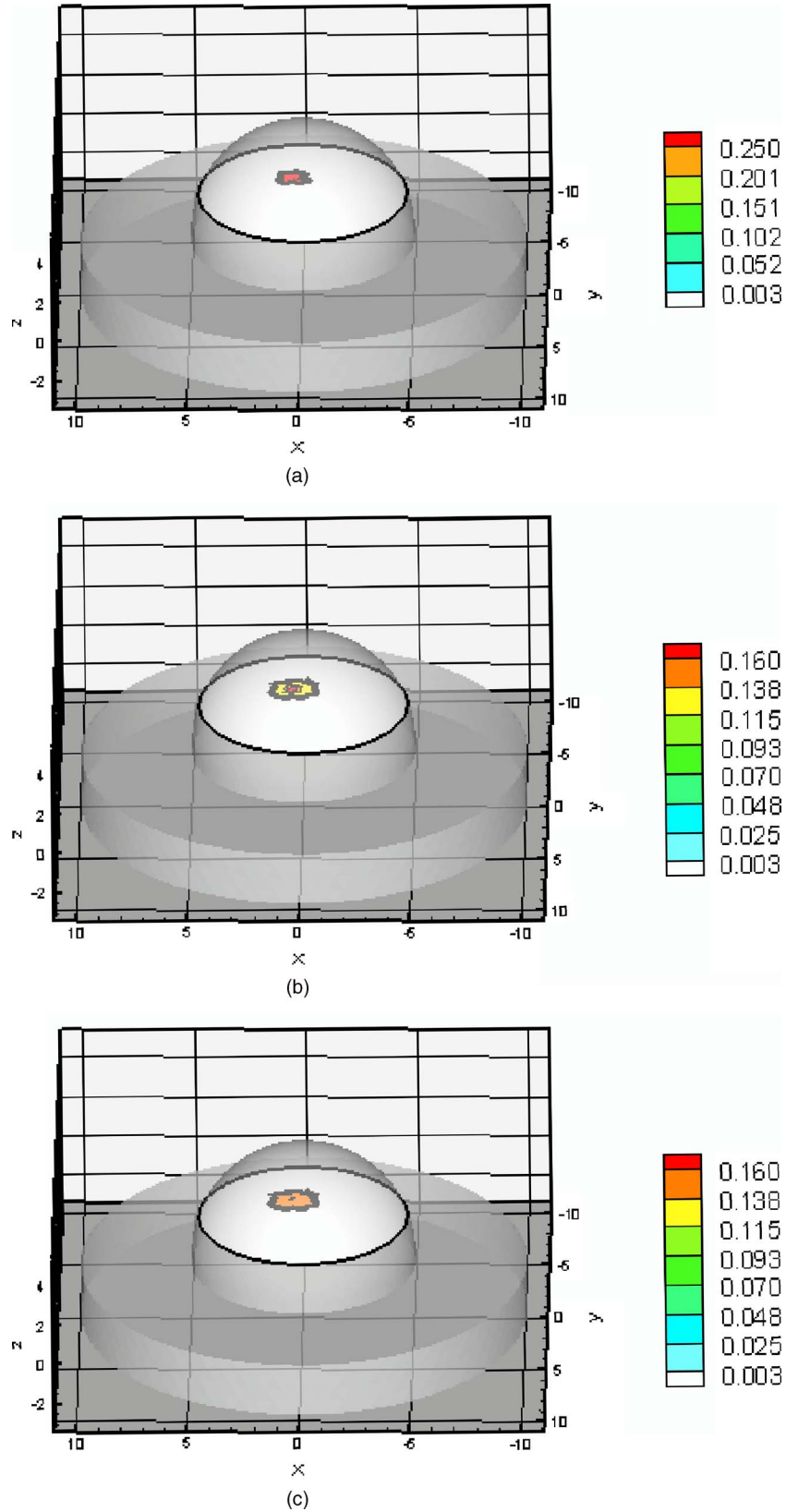


Fig. 5 Distribution of absorption coefficient due to fluorophore $\mu_{a_{xf}} \text{ cm}^{-1}$ with 1.0 cm^3 spherical target located at 2.8 cm deep (centroid $0.5, -1.5, 1.5$) under perfect uptake condition at $Z=1.4\text{-cm}$ plane through the target, (a) actual distribution of the absorption coefficient due to fluorophore, (b) reconstructed image using initial value $\mu_{a_{xf}}^0=0.003 \text{ cm}^{-1}$ and $\lambda^0=1000$, (c) reconstructed image using initial value $\mu_{a_{xf}}^0=0.003 \text{ cm}^{-1}$ and calculated λ^0 (experiment #5, Mesh 2).

Table 4 Summary of figures of targets reconstruction, CPU time, and the root mean square error (RMSE) as a function of initial value of the absorption coefficient due to fluorophore $\mu_{a,xf}^0 = 0.003$ and 0.002 cm^{-1} and the initial Lagrange multiplier $\lambda^0 = 1000$ as well as calculated λ^0 (Ref. 28) for perfect and imperfect uptake measurements (Experiments #5–6) using Mesh 1 and Mesh 2.

| Exp. | Lagrange λ^0 | Time (min.) | Centroid [xyz] (cm) | RMSE ^b | Mesh ^c | Volume (cm ³) | Max ^f $\mu_{a,xf}$ (cm ⁻¹) |
|----------------|----------------------|-------------|---------------------|-------------------|-------------------|---------------------------|---|
| 5 ^d | Actual | | 0.5–1.5 1.5 | | 1 | 1.0 | 0.3 |
| | $\lambda^0 = 1000$ | 23 | 0.4–1.5 1.5 | 0.0148 | 1 | 3.0 | 0.18 |
| | Cal λ^{0a} | 29 | 0.4–1.5 1.5 | 0.0134 | 1 | 3.1 | 0.17 |
| 6 ^d | Actual | | 0.5–1.5 1.5 | | 1 | 1.0 | 0.3 |
| | $\lambda^0 = 1000$ | 28 | 0.4–1.5 1.5 | 0.0145 | 1 | 3.0 | 0.18 |
| | Cal λ^{0a} | 45 | 0.4–1.5 1.5 | 0.0137 | 1 | 3.1 | 0.17 |
| 5 ^d | Actual | | 0.5–1.5 1.5 | | 2 | 1.0 | 0.3 |
| | $\lambda^0 = 1000$ | 100 | 0.4–1.5 1.5 | 0.0128 | 2 | 1.9 | 0.19 |
| | Cal λ^{0a} | 170 | 0.4–1.5 1.5 | 0.0120 | 2 | 1.9 | 0.18 |
| 6 ^d | Actual | | 0.5–1.5 1.5 | | 2 | 1.0 | 0.3 |
| | $\lambda^0 = 1000$ | 130 | 0.4–1.5 1.5 | 0.0129 | 2 | 1.8 | 0.18 |
| | Cal λ^{0a} | 230 | 0.4–1.5 1.5 | 0.0119 | 2 | 1.9 | 0.19 |
| 6 ^e | Actual | | 0.5–1.5 1.5 | | 1 | 1.0 | 0.3 |
| | Cal λ^{0a} | 43 | 0.4–1.5 1.5 | 0.0176 | 1 | 3.1 | 0.17 |

^aUsing calculated Lagrange multiplier λ_i^0 (Ref. 28).
^bRoot mean square error (RMSE, Eq. (10)).
^cMesh 1 (coarse) with 6956 nodes, Mesh 2 (fine) with 18,105 nodes.
^dLower and upper bound (0.003, 0.3).
^eLower and upper bounds (0.002, 0.4).
^fMaximum absorption coefficient due to fluorophore in the target region.

The inner iteration is completed when the value of the barrier function is very small and further decrease is not possible. To summarize, the PMBF method with simple bounds on the optical properties of the tissue provides fast access to image recovery.

It is seen from Fig. 4 that the reconstructed targets are at the “true” location but larger in size. This may be due to large mesh sizes. To investigate this, a finer mesh (Mesh 2) was used. Figure 5 shows the recovery of absorption coefficient due to fluorophore by the PMBF/CONTN algorithm using the measurement data of experiment #5, i.e., a 10-cm³ spherical target embedded 2.8 cm deep (centroid 0.5, -1.5, 1.5). Figure 5(a) shows the true distribution of the absorption coefficient due to fluorophore in Z=1.4-cm plane through the target while Fig. 5(b) is the reconstructed images in Z=1.4-cm plane through the target using the initial Lagrange multiplier $\lambda^0 = 1000$. Figure 5(c) is reconstructed in Z=1.4-cm plane through the target using the initial Lagrange multipliers λ^0 computed using the method of Breitfeld and Shanno.³⁹ The quantitative measures associated with the reconstructed images are listed in Tables 3 and 4. It is seen in Tables 3 and 4 that the volume of the reconstructed target is smaller in the

fine mesh than that of coarse mesh. The volumes of the constructed targets are larger than the true volumes under conditions of imperfect uptake. Thus, the results show that a finer mesh provides a reconstructed volume closer to the actual volume. However, it is seen from Figs. 4 and 5 that the locations of the reconstructed images using both fine and coarse the finite element meshes are at the same locations as ground truth. As before, the centroids of the reconstructed targets using finer mesh are close to their true locations as given in Table 4. The maximum values of the absorption coefficients due to fluorophore in the reconstructed targets region and the true values are given in Tables 3 and 4, which show that these values are closer to true values when a fine mesh used. The RSME using the fine mesh was slightly less than that of coarse mesh. Time required to reconstruct a target at 2.8 cm deep using the computed Lagrange multipliers on the Mesh 2 was 3 hr 50 min and on Mesh 1 was 45 min (Tables 3 and 4). The time required to reconstruct the same sized target placed at 2 cm deep using the computed Lagrange multiplier on Mesh 2 was 2 hr 50 min while on Mesh 1 it took 29 min. Thus we see that the CPU time required for target reconstruction increases as the number of measurements increases, the

target becomes deeper, and the mesh more refined.

We have demonstrated that the PMBF/CONTN reconstructed the targets accurately when the lower bound and the upper bounds of the absorption coefficient due to fluorophore, $\mu_{a_{xf}}$, were 0.003 and 0.3 cm^{-1} , respectively, and the initial value of $\mu_{a_{xf}}$ were between the lower and upper bounds. In order to investigate the influence of the lower and upper bounds on the performance of the algorithm PMBF/CONTN, the lower bound and the upper bound of $\mu_{a_{xf}}$ were chosen to be 0.002 cm^{-1} and 0.4 cm^{-1} , respectively, and the initial values of $\mu_{a_{xf}}$ were between these bounds. Figure 6 illustrates the recovery of absorption coefficient due to fluorophore by the PMBF/CONTN algorithm using the measurement data of experiment #6, i.e., a 1.0- cm^3 spherical target embedded in 2.8 cm deep (centroid 0.5, -1.5, 1.5) under imperfect uptake. Figure 6(a) shows the actual distribution of the absorption coefficient due to fluorophore in $Z=1.4$ -cm plane through the target. Figure 6(b) demonstrates the reconstructed target in $Z=1.4$ -cm plane through the target using an initial guess of uniform $\mu_{a_{xf}}^0$ to be 0.002 cm^{-1} and the initial Lagrange multiplier λ^0 calculated by the modified method of Breitfeld and Shanno³⁹ (results of experiment #1 using the same lower and upper bounds are given in Table 3). The CPU time required for both these cases and the RMSE, location, and size of the target are nearly the same (Tables 3 and 4). Thus we have seen the efficiency and accuracy of the PMBF/CONTN algorithm do not depend on the values of the lower and upper bounds providing these values based on physical considerations.

In summary, the target depth studies demonstrated the capability of the algorithm to accurately detect single 1.0- cm^3 spherical targets located up to 2.8 cm deep under both perfect and imperfect conditions.

3.3 Small Target Reconstruction (Single and Multiple Spherical Targets)

The absorption coefficient due to the fluorescent $\mu_{a_{xf}}$ was reconstructed for experiments #7–8. Figure 7 illustrates in plane through $Z=2.4$, the PMBF recovery of absorption coefficient due to fluorophore from referenced fluorescent measurements made under perfect uptake conditions for experiment #8 (similar results were obtained using experiment #7). Table 5 summarizes all the computed runs of experiments #7–8. Figure 7(a) corresponds to the actual spatial distribution of fluorescence absorption coefficient, $\mu_{a_{xf}}$, when multiple spherical targets of volume $\sim 0.55 \text{ cm}^3$ were placed 1.4 cm away from the surface. Figure 7(b) demonstrates the reconstructed target using an initial guess of uniform $\mu_{a_{xf}}^0$ to be 0.003 cm^{-1} and the initial Lagrange multipliers chosen to be $\lambda_i^0=1000$. As before, we also found that the initial Lagrange multiplier of $\lambda_i^0=1, 10$, and 100 resulted in smaller target sizes and displaced reconstructed targets locations without artifacts. Figure 7(c) shows the reconstructed targets using the computed value of λ_i^0 . These results were obtained using Mesh 1. In each case the reconstructed single and multiple targets were clearly distinguishable from surroundings without artifacts and the sizes of the reconstructed targets were smaller than the true targets. The centroid of the reconstructed targets and the actual location of the targets are given in Table

5. However, the targets were reconstructed close to their actual location with no artifacts as shown in Fig. 7.

As before, we also used the fine mesh (Mesh 2) for image reconstruction. Figure 8 shows the recovery of absorption coefficients $\mu_{a_{xf}}$ of three targets in plane through $Z=2.4$. Figure 8(a) shows the true distribution of the absorption coefficient due to fluorophore while Fig. 8(b) illustrates the reconstructed targets using the initial Lagrange multiplier of $\lambda^0=1000$. Figure 8(c) was reconstructed using the computed λ^0 . It is seen that the volume of the reconstructed targets in the fine mesh slightly smaller than that of coarse mesh (Table 5). Hence the results show that a finer mesh provides a reconstructed volume closer to the actual volume. They also show that the maximum absorption coefficients in the target region are slightly smaller using the fine mesh rather than the coarse mesh. That is, the reconstructed values are closer to the true values as the mesh was refined. This shows that we need finer meshes as the depth of the target increase. However, the locations of the reconstructed images using both the finite element meshes were at the same locations as the true images. The RSME using the fine mesh was slightly less than that of the coarse mesh (Table 5). Again, more CPU time was required when the initial value of λ^0 were calculated (Table 5). However, it should be noted that the overall CPU times could be higher if the trial-and-error method to find the Lagrange multipliers was used.

Both PMBF/CONTN and a Bayesian approach (AEKF)⁴¹ were used for the breast-shaped phantom studies. The referenced fluorescence measurement of intensity and phase shift were used in both algorithms to find the 3-D map of absorption coefficient due to fluorophore in the interior of the phantom. Details of the Bayesian method have presented elsewhere.⁴¹ To compare the performance of both algorithms, we have calculated the volumes of the reconstructed targets and found the centroid locations of the reconstructed targets. Results of experiments #2, 4, 6, and 8 using AEKF are discussed in Ref. 41. It was found that the reconstructed image using the AEKF was slightly shifted from the original location (Table 3 in Ref. 41) while the PMBF/CONTN reconstructed the images at the close to actual location as given in Table 6. It was found that the AEKF underestimated the actual depth of the target as the depth increases.⁴¹ It was stated in Ref. 41 that the volume of the reconstructed target was sensitive to the threshold value of the reconstructed parameter and the threshold values were problem-dependent. The threshold value obtained for each experimental data has no mathematical foundation and was found from ground truth. A minimum-variance approach is used in the AEKF method. In this method the measurement error covariance and dynamically estimated parameter error covariance are used for the regularization of the ill-conditioned problem. While in the PMBF/CONTN method, the barrier and Lagrange multipliers regularize the solution. The PMBF method will converge, providing the Lagrange multipliers are positive.³⁸ Furthermore, an active constrained optimization method is utilized. In this method we divide the optimization variables in three parts based upon their local gradients, and accordingly these variables satisfy the lower and the upper bounds conditions.²⁸ Hence there is no threshold required. We have seen that volumes of the reconstructed images are slightly higher than the actual volume

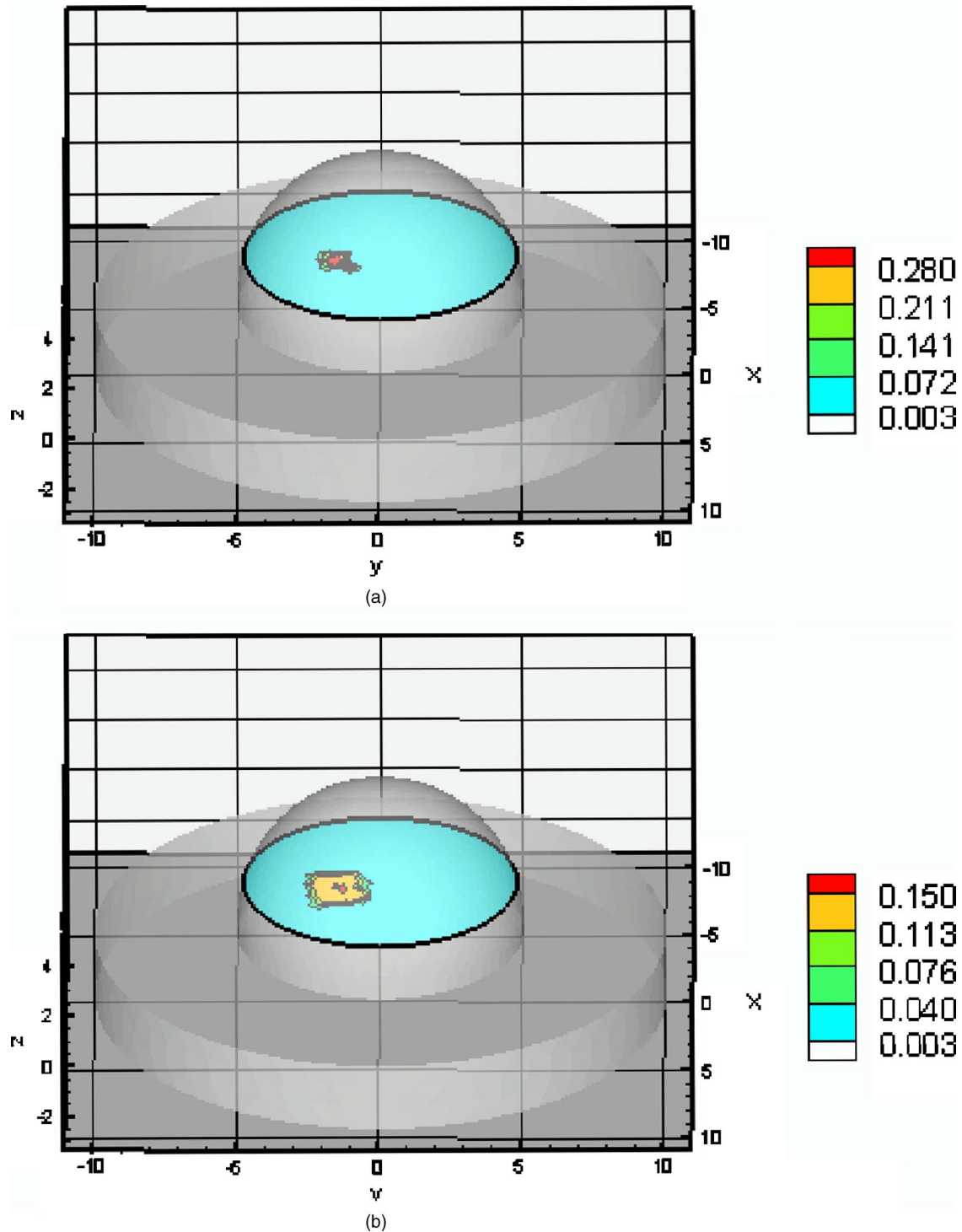


Fig. 6 Distribution of absorption coefficient due to fluorophore $\mu_{a_{xf}}$ cm^{-1} with 1.0 cm^3 spherical target located at 2.8 cm deep (centroid $0.5, -1.5, 1.5$) from the surface under imperfect uptake condition at $Z=1.4\text{-cm}$ plane through the target, (a) actual distribution of the absorption coefficient due to fluorophore, (b) reconstructed image using initial value $\mu_{a_{xf}}^0=0.002 \text{ cm}^{-1}$ and calculated λ^0 (experiment #6, Mesh 1).

using a coarse mesh (Mesh 1), but the volumes reduced considerably when a fine mesh (Mesh 2) was used.

Figures 3–5 in Ref. 41 showed there are some artifact effects using the experiments data specifically for imperfect uptake (T:B ratio, 100:1) with 10 cm^3 spherical target located 2.04 and 2.82 cm deep. The artifacts increase as the depth of

the target increases. We have seen in Figs. 6 and 7 in Ref. 41 that the artifacts were very high when three targets were reconstructed while the PMBF method reconstructed images without artifacts as shown in Figures 4–8.

To summarize, we have demonstrated that the algorithm based on the PMBF method with constrained optimization

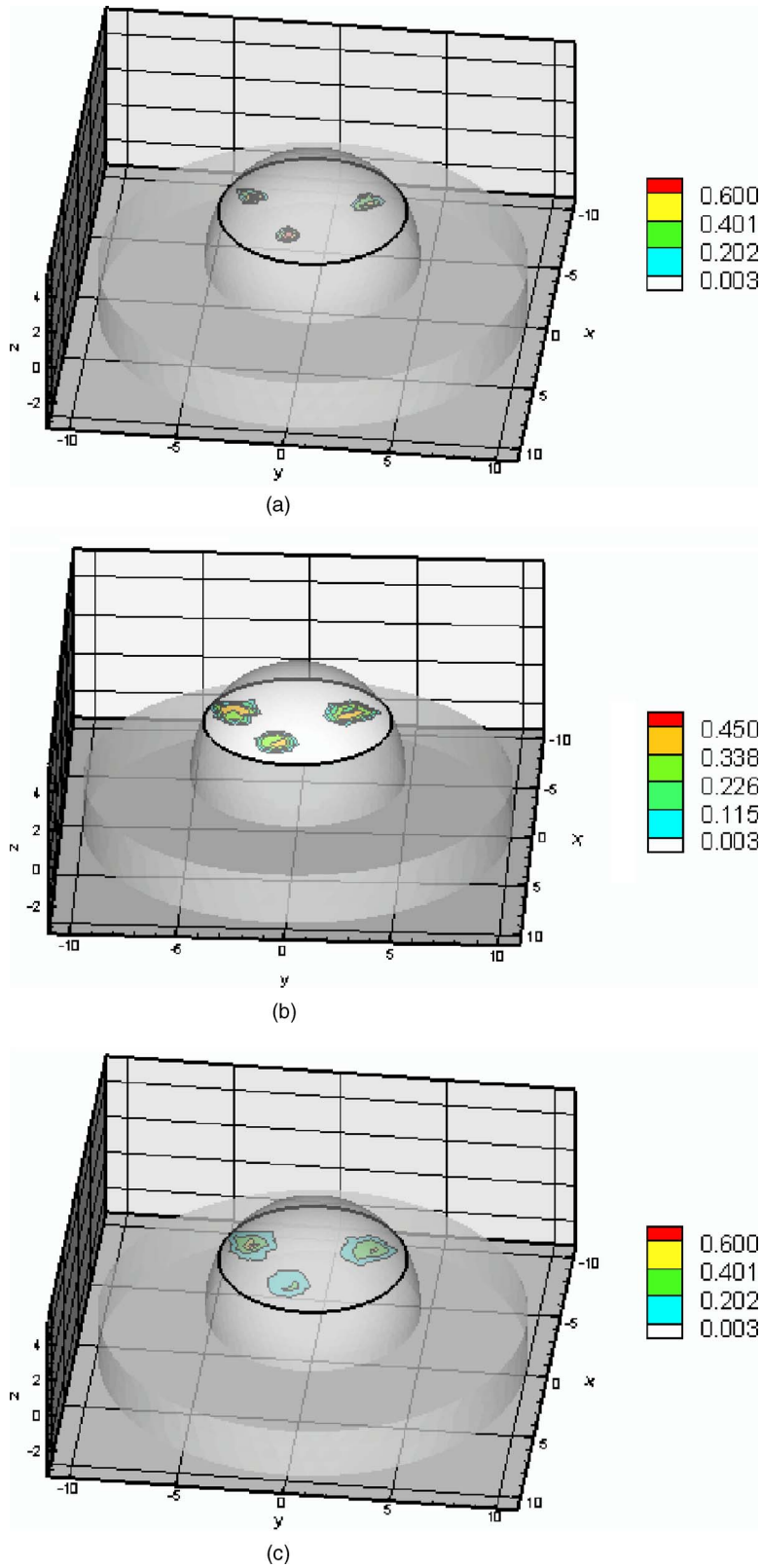


Fig. 7 Distribution of absorption coefficient due to fluorophore $\mu_{a_{xf}} \text{ cm}^{-1}$, three spherical targets of volumes $0.5\text{--}0.6 \text{ cm}^3$ located $1.2\text{--}1.4 \text{ cm}$ deep from the surface (centroids, $-1.0, -3.0, 1.8$; $-1.0, 2.0, 2.9$; $2.0, -1.0, 3.0$) under perfect uptake condition at $Z=2.4\text{-cm}$ plane through the targets, (a) actual distribution of the absorption coefficient due to fluorophore, (b) reconstructed image using initial value $\mu_{a_{xf}}^0=0.003 \text{ cm}^{-1}$ and $\lambda^0=1000$, (c) reconstructed image using initial value $\mu_{a_{xf}}^0=0.003 \text{ cm}^{-1}$ and calculated λ^0 (experiment #8, Mesh 1).

Table 5 Summary of figures of targets reconstruction, CPU time, and the root mean square error (RMSE) as a function of initial value of the absorption coefficient due to fluorophore $\mu_{a,xf}^0 = 0.003 \text{ cm}^{-1}$ and the initial Lagrange multiplier $\lambda^0 = 1000$ as well as calculated λ^0 (Ref. 28) for perfect uptake measurements (Experiments #7–8) using Mesh 1 and Mesh 2.

| Exp. | Lagrange λ^0 | Time (min.) | Centroid [xyz] (cm) | RMSE ^b | Mesh ^c | Volume (cm ³) | Max ^f $\mu_{a,xf}$ (cm ⁻¹) | |
|----------------|----------------------|--------------------|---------------------|-------------------|-------------------|---------------------------|---|-------|
| 7 ^d | Actual | | -0.5–2.5 1.5 | | 1 | ~0.5 | 0.3 | |
| | $\lambda^0 = 1000$ | 26 | -0.5–2.4 1.4 | 0.010 | 1 | 0.9 | 0.16 | |
| | Cal λ^{0a} | 30 | -0.6–2.5 1.5 | 0.010 | 1 | 0.9 | 0.17 | |
| 7 ^d | Actual | | -0.5–2.5 1.5 | | 2 | ~0.5 | 0.3 | |
| | $\lambda^0 = 1000$ | 60 | -0.6–2.5 1.6 | 0.005 | 2 | 0.8 | 0.18 | |
| | Cal λ^{0a} | 170 | -0.6–2.5 1.6 | 0.005 | 2 | 0.8 | 0.17 | |
| 8 ^e | Actual | | -1.0–3.0 1.8 | | 1 | ~0.55 | 0.747 | |
| | | | -1.0 2.0 2.9 | | | ~0.55 | 0.747 | |
| | | | 2.0 -1.0 3.0 | | | ~0.55 | 0.747 | |
| | $\lambda^0 = 1000$ | 24 | -0.9 -2.9 1.8 | 0.048 | 1 | 0.95 | 0.373 | |
| | | | -0.8 2.9 2.8 | 0.049 | | 0.91 | 0.358 | |
| | | | 1.9 -1.0 2.9 | 0.047 | | 0.95 | 0.373 | |
| | Cal λ^{0a} | 31 | -0.9 -2.8 1.8 | 0.039 | 1 | 0.92 | 0.0388 | |
| | | | -0.8 1.8 2.8 | 0.040 | | 0.96 | 0.393 | |
| | | | 1.8 -1.0 2.9 | 0.042 | | 0.95 | 0.403 | |
| 8 ^e | Actual | | | | 2 | | | |
| | | $\lambda^0 = 1000$ | 110 | -1.0 -2.9 1.8 | 0.0437 | 2 | 0.81 | 0.400 |
| | | | | -1.0 1.9 2.8 | 0.0425 | | 0.88 | 0.410 |
| | | | 1.9 -1.0 2.9 | 0.0438 | | 0.87 | 0.420 | |
| | Cal λ^{0a} | 190 | -1.0 -2.9 1.8 | 0.0412 | 2 | 0.88 | 0.480 | |
| | | | | -1.0 1.9 2.8 | 0.0423 | | 0.86 | 0.491 |
| | | 1.9 -0.9 2.9 | 0.0412 | | 0.85 | 0.472 | | |

^aUsing calculated Lagrange multiplier λ_i^0 (Ref. 28).

^bRoot mean square error (RMSE, Eq. (10)).

^cMesh 1 (coarse) with 6956 nodes, Mesh 2 (fine) with 18,105 nodes and 94,767.

^dLower and upper bound (0.003, 0.3).

^eLower and upper bounds (0.003, 747).

^fMaximum absorption coefficient due to fluorophore in the target region.

technique (CONTN) and the combination of the modified Breitfeld and Shanno method to calculate the Lagrange multipliers successfully reconstructs targets close to their true locations without artifacts for all the eight different experimental cases.

4 Conclusions

A novel, computationally efficient penalty-modified barrier function method and simple bound constrained truncated

Newton with trust region method was used for fluorescence-enhanced optical tomography using point illumination/collection geometries. For diagnostic and prognostic breast imaging, an algorithm should be developed so that it is capable of reconstructing single and multiple targets of small volumes at different locations in a large tissue volume. With these objectives in mind, we demonstrate that our algorithm reconstructs targets of different sizes embedded at different locations of the phantom of clinically relevant volume. The

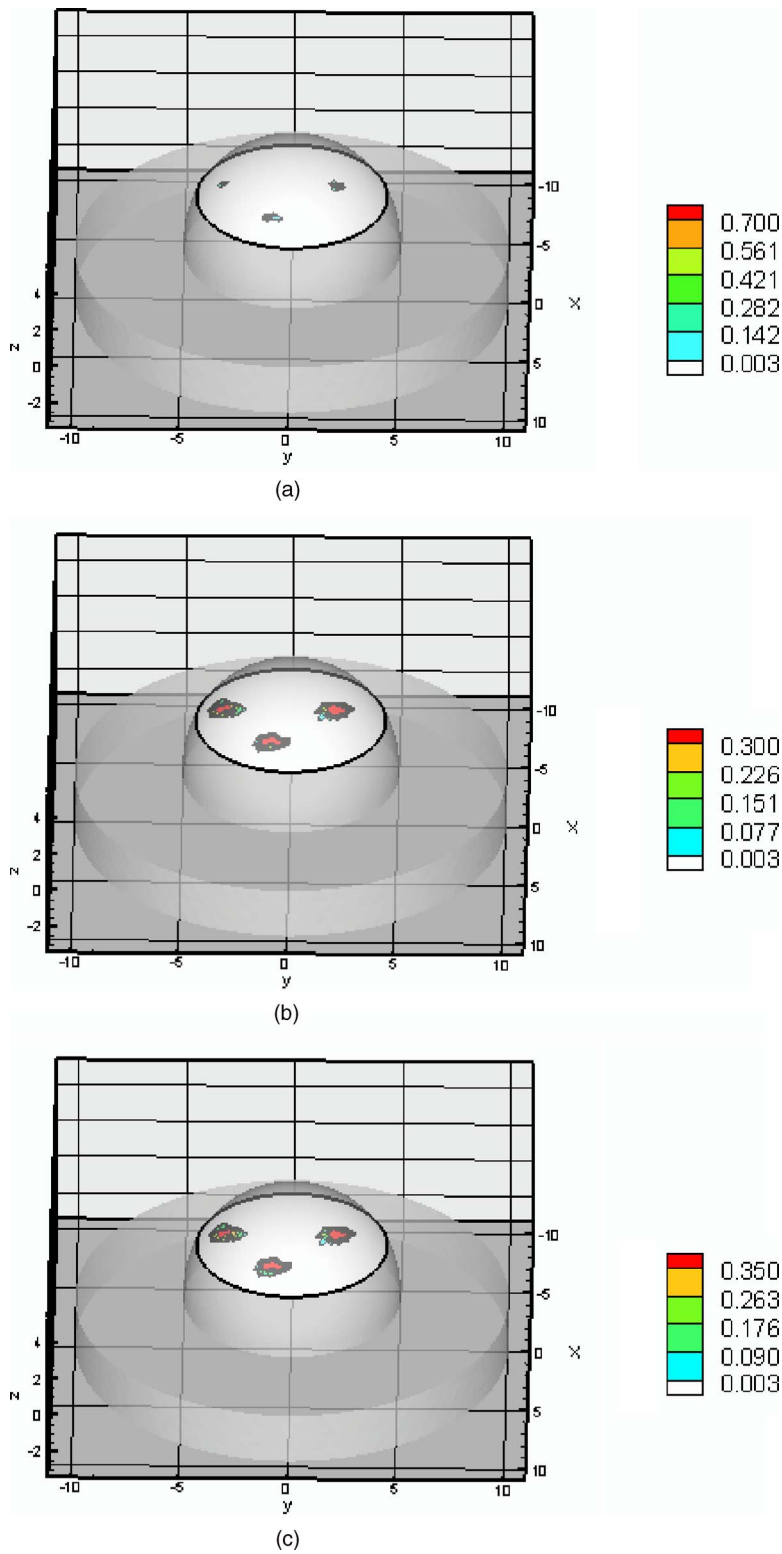


Fig. 8 Distribution of absorption coefficient due to fluorophore $\mu_{a_{xf}} \text{ cm}^{-1}$, three spherical targets of volumes $0.5\text{--}0.6 \text{ cm}^3$ located $1.2\text{--}1.4 \text{ cm}$ deep from the surface (centroids, $-1.0, -3.0, 1.8$; $-1.0, 2.0, 2.9$; $2.0, -1.0, 3.0$) under perfect uptake condition at $Z=2.4\text{-cm}$ plane through the targets, (a) actual distribution of the absorption coefficient due to fluorophore, (b) reconstructed image using initial value $\mu_{a_{xf}}^0=0.003 \text{ cm}^{-1}$ and $\lambda^0=1000$, (c) reconstructed image using initial value $\mu_{a_{xf}}^0=0.003 \text{ cm}^{-1}$ and calculated λ^0 (experiment #8, Mesh 2).

Table 6 Targets centroids and volumes calculated by PMBF/CONTN and AEKF.

| Exp. | Target's Centroid [xyz] (cm) | | | Target's Volume (cm ³) | | |
|------|------------------------------|---|--|------------------------------------|-------------------|----------------|
| | Actual | AEKF ^a (difference in centroid location cm) | PMBF/ CONTN (difference in centroid location cm) | Actual | AEKF ^a | PMBF/ CONTN |
| 2 | 0.5, -2.5 2.5 | 0.31 | 0.0 | 1.0 | 1.0 | 2.5 |
| 4 | 0.5 -1.5 2.5 | 0.64 | 0.1 | 1.0 | 3.2 | 1.9 |
| 6 | 0.5 -1.5 1.5 | 1.5 | 0.1 | 1.0 | 2.6 | 3.0 |
| | -1.0 -3.0 1.8 | 0.46 | 0.1 | ~0.55 | 0.2 | 0.98 |
| 8 | -1.0 2.0 2.9 | 0.21 | 0.15 | ~0.55 | 1.6 | 0.99 |
| | 2.0 -1.0 3.0 | 0.06 | 0.15 | ~0.55 | 0.9 | 0.99 |

^aRef. 41.

combination of penalty barrier function method and simple bound constrained method makes the algorithm efficient and the use of the Breitfeld and Shanno method for computing the initial Lagrange multipliers removed the need to have *a priori* information. It was shown that the algorithm can reconstruct completely accurate images to its true locations without artifacts using measurements that have a low single to noise ratio (SNR) as well as high discretization error in forward solution. We have used image RMSE as quantitative measures of a spatially varying absorption coefficient due to fluorophore in order to produce a compact summary that could easily be compared across the large number of images produced in this study. The performance of the algorithm was not affected by the choice of the initial guess of the absorption coefficient due to fluorophore as long as the initial value lies within the lower and the upper bounds. Furthermore, the algorithm is not geometry-dependent, since it has been successfully used to reconstruct 3-D images from 2-D area illumination and area detection measurement.²⁸ Our demonstration of image reconstruction was implemented under perfect and imperfect condition and with depth of penetrations up to 2.8 cm, and the volume of the smallest spherical target was 0.5 cm³. Future work will focus on reconstruction of targets of volumes less than 0.5 cm³ and at greater depths than 2.8 cm with multiple targets, and with lower concentration of the fluorophore. In order to accomplish these goals, improvement in excitation light rejection is required.

Acknowledgment

The research was supplied by National Institutes of Health (NIH R21 EB000885). We thank Margaret Eppstein for her finite element meshes used in this paper.

References

1. S. R. Arridge, "Optical tomography in medical imaging," *Inverse Probl.* **15**, R41–R93 (1999).
2. D. A. Boas, D. H. Brooks, E. L. Miller, C. A. DiMarzio, M. Kilmer, R. J. Gaudette, and Q. Zhang, "Imaging the body with diffuse optical tomography," *IEEE Signal Process. Mag.* **18**, 57–75 (2001).
3. A. D. Klose, U. Netz, J. Beuthan, and A. H. Hielscher, "Optical tomography using the time-independent equation of radiative transfer—Part 1: Forward model," *J. Quant. Spectrosc. Radiat. Transf.* **72**, 691–713 (2002).
4. A. D. Klose and A. H. Hielscher, "Optical tomography using the time-independent equation of radiative transfer—Part 2: Inverse mode," *J. Quant. Spectrosc. Radiat. Transf.* **72**, 715–732 (2002).
5. B. W. Pogue, S. Geimer, T. O. McBride, S. D. Jiang, U. L. Osterberg, and K. D. Paulsen, "Three-dimensional simulation of near-infrared diffusion in tissue: Boundary condition and geometry analysis for finite-element image reconstruction," *Appl. Opt.* **40**, 588–600 (2001).
6. B. W. Pogue, S. P. Poplack, T. O. McBride, W. A. Wells, K. S. Osterman, U. L. Osterberg, and K. D. Paulsen, "Quantitative hemoglobin tomography with diffuse near-infrared spectroscopy: Pilot results in the breast," *Radiology* **218**, 261–266 (2001).
7. S. B. Colak, M. B. van der Mark, G. W. 't Hooft, J. H. Hoogenraad, E. S. van der Linden, and F. A. Kuijpers, "Clinical optical tomography and NIR spectroscopy for breast cancer detection," *IEEE J. Sel. Top. Quantum Electron.* **5**, 1143–1158 (1999).
8. H. Jiang, Y. Xu, N. Iftimia, J. Eggert, K. Klove, L. Baron, and L. Fajardo, "Three-dimensional optical tomographic imaging of breast in a human subject," *IEEE Trans. Med. Imaging* **20**, 1334–1340 (2001).
9. D. Grosenick, H. Wabnitz, H. H. Rinneberg, K. T. Moesta, and P. M. Schlag, "Development of a time-domain optical mammograph and first *in vivo* applications," *Appl. Opt.* **38**, 2927–2943 (1999).
10. K. T. Moesta, S. Fantini, H. Jess, S. Totkas, M. A. Franceschini, M. Kaschke, and P. M. Schlag, "Contrast features of breast cancer in frequency-domain laser scanning mammography," *J. Biomed. Opt.* **3**, 129–136 (1998).
11. D. J. Hawrysz and E. M. Sevick-Muraca, "Developments toward diagnostic breast cancer imaging using near-infrared optical measurements and fluorescent contrast agents," *Neoplasia* **2**, 388–417 (2000).
12. E. M. Sevick-Muraca, A. Godavarty, J. P. Houston, A. B. Thompson, and R. Roy, "Near-infrared imaging with fluorescent contrast agents," in *Handbook of Biomedical Fluorescence*, B. W. Pogue and M. A. Mycek, Eds., Marcel Dekker Inc., New York, pp. 445–527 (2003).
13. J. P. Houston, A. B. Thompson, M. Gurfinkel, and E. M. Sevick-Muraca, "Sensitivity and depth penetration of continuous wave *versus* frequency-domain photon migration near-infrared fluorescence contrast-enhanced imaging," *Photochem. Photobiol.* **77**, 420–430 (2003).
14. E. M. Sevick-Muraca, G. Lopez, T. Troy, J. S. Reynolds, and C. L. Hutchinson, "Fluorescence and absorption contrast mechanisms for biomedical optical imaging using frequency-domain techniques," *Photochem. Photobiol.* **66**, 55–64 (1997).
15. X. Li, B. Chance, and A. G. Yodh, "Fluorescence heterogeneities in

- turbid media, limits for detection, characterization, and comparison with absorption," *Appl. Opt.* **37**, 6833–6843 (1998).
16. J. Lee and E. M. Sevick-Muraca, "Fluorescence enhanced absorption imaging: Noise tolerance characteristics compared with conventional absorption and scattering imaging," *J. Biomed. Opt.* **6**, 58–67 (2001).
 17. V. Chernomordik, D. Hattery, I. Gannot, and A. H. Gandjbakhche, "Inverse method 3-D reconstruction of localized *in vivo* fluorescence—application to Sjogren syndrome," *IEEE J. Sel. Top. Quantum Electron.* **54**, 930–935 (1999).
 18. V. Ntziachristos and R. Weissleder, "Experimental three-dimensional fluorescence reconstruction of diffuse media by use of a normalized Born approximation," *Opt. Lett.* **26**, 893–895 (2001).
 19. V. Ntziachristos and R. Weissleder, "Charged-couple-device based scanner for tomography of fluorescent near-infrared probes in turbid media," *Med. Phys.* **29**, 893–895 (2002).
 20. Y. Yang, N. Iftimia, Y. Xu, and H. Jiang, "Frequency-domain fluorescent diffusion tomography of turbid media and *in vivo* tissues," *Proc. SPIE* **4250**, 537–545 (2001).
 21. E. L. Hull, M. G. Nichols, and T. H. Foster, "Localization of luminescent inhomogeneities in turbid media with spatially resolved measurements of CW diffuse luminescence emittance," *Appl. Opt.* **37**, 2755–2765 (1998).
 22. D. J. Hawrysz, M. J. Eppstein, J. Lee, and E. M. Sevick-Muraca, "Error consideration in contrast-enhanced three-dimensional optical tomography," *Opt. Lett.* **26**, 704–706 (2001).
 23. M. J. Eppstein, D. J. Hawrysz, A. Godavarty, and E. M. Sevick-Muraca, "Three-dimensional, near-infrared fluorescence tomography with Bayesian methodologies for image reconstruction from sparse and noisy data sets," *Proc. Natl. Acad. Sci. U.S.A.* **99**, 9619–9624 (2002).
 24. J. Lee and E. M. Sevick-Muraca, "3-D Fluorescence enhanced optical tomography using referenced frequency-domain photon migration measurements at emission and excitation measurements," *J. Opt. Soc. Am. A* **19**, 759–771 (2002).
 25. K. Hwang, J. P. Houston, J. C. Rasmussen, A. Joshi, S. Ke, C. Li, and E. M. Sevick-Muraca, "Improved excitation light rejection enhances small animal fluorescence optical imaging," *Mol. Imaging* **4**, 194–204 (2005).
 26. S. B. Colak, M. B. van der Mark, G. W. 't Hooft, J. H. Hoogenraad, E. S. van der Linden, and F. A. Kuijpers, "Clinical optical tomography and NIR spectroscopy for breast cancer detection," *IEEE J. Sel. Top. Quantum Electron.* **5**, 1143–1179 (1999).
 27. A. Joshi, W. Bangerth, and E. M. Sevick-Muraca, "Adaptive finite element based tomography for fluorescence optical imaging in tissue," *Opt. Express* **112**, 5402–5417 (2004).
 28. R. Roy, A. B. Thompson, A. Godavarty, and E. M. Sevick-Muraca, "Tomographic fluorescence imaging in tissue phantoms: A novel reconstruction algorithm and imaging geometry," *IEEE Trans. Med. Imaging* **24**, 137–154 (2005).
 29. R. Roy and E. M. Sevick-Muraca, "Truncated Newton's optimization scheme for absorption and fluorescence optical tomography: Part I, Theory and Formulation," *Opt. Express* **4**, 353–371 (1999).
 30. A. Godavarty, M. J. Eppstein, C. Zhang, S. Theru, A. B. Thompson, M. Gurfinkel, and E. M. Sevick-Muraca, "Fluorescence-enhanced optical imaging in large tissue volumes using a gain modulated ICCD camera," *Phys. Med. Biol.* **48**, 1701–1720 (2003).
 31. A. Godavarty, C. Zhang, M. J. Eppstein, and E. M. Sevick-Muraca, "Fluorescence-enhanced optical imaging in large phantoms using single and simultaneous dual point illumination geometries," *Med. Phys.* **31**, 183–190 (2004).
 32. A. B. Thompson and E. M. Sevick-Muraca, "Near-infrared fluorescence contrast enhanced imaging with intensified charge-coupled device homodyne detection: Measurement precision and accuracy," *J. Biomed. Opt.* **8**, 111–120 (2003).
 33. R. Roy, A. Godavarty, and E. M. Sevick-Muraca, "Fluorescence-enhanced, optical tomography using referenced measurements of heterogeneous media," *IEEE Trans. Med. Imaging* **22**, 824–836 (2003).
 34. A. Ishimaru, *Wave Propagation and Scattering in a Random Media*, Academic Press, New York (1978).
 35. R. Roy and E. M. Sevick-Muraca, "Active constrained truncated Newton method for simple-bound optical tomography," *J. Opt. Soc. Am. A* **17**, 1627–1641 (2000).
 36. R. Roy and E. M. Sevick-Muraca, "Three-dimensional unconstrained and constrained image reconstruction techniques applied to fluorescence, frequency-domain photon migration," *Appl. Opt.* **40**, 2206–2215 (2001).
 37. A. N. Tikhonov and V. Y. Arsenin, *Solution of Ill-Posed Problems*, V. H. Winston & Sons, Washington, DC (1977).
 38. R. Polyak, "Modified barrier function (theory and methods)," *Math. Program.* **54**, 177–222 (1992).
 39. M. G. Breitfeld and D. F. Shanno, "Computational experience with penalty-barrier methods for nonlinear programming," *Ann. Operat. Res.* **62**, 439–463 (1996).
 40. T. W. C. Chen and V. S. Vassiliadis, "Solution of general nonlinear optimization problem using the penalty/barrier method with the use of exact Hessians," *Comput. Chem. Eng.* **27**, 501–525 (2003).
 41. A. Godavarty, M. J. Eppstein, C. Zhang, and E. M. Sevick-Muraca, "Detection of single and multiple targets in tissue phantoms with fluorescence-enhanced optical imaging: Feasibility study," *Radiology* **235**, 148–154 (2005).